Journal Name

COMMUNICATION

Mechanism of water oxidation by [Ru(bda)(L)$_2$]: the return of the "blue dimer"

Cite this: DOI: 10.1039/xoxxoooooox

Javier J. Concepcion,*[a] Diane K. Zhong,[a,c] David J. Szalda,[b] James T. Muckerman,[a] Etsuko Fujita[a]

Received ooth January 2012,
Accepted ooth January 2012

DOI: 10.1039/xoxxoooooox

We describe here a combined solution-surface-DFT calculations study for complexes of the type [Ru(bda)(L)$_2$] including X-ray structure of intermediates, their reactivity, as well as pH-dependent electrochemistry and spectroelectrochemistry. These studies shed light on the mechanism of water oxidation by [Ru(bda)(L)$_2$], revealing key features unavailable from solution studies with sacrificial oxidants.

Natural photosynthesis has sustained life on Earth for billions of years. Water oxidation is a key component in this essential process. It provides the redox equivalents and protons that ultimately lead to accumulation of solar energy in chemical bonds. Many potential solutions to cover our growing energy demands and to reduce damage to the environment involve solar-driven water oxidation. But this requires efficient and robust water oxidation catalysts.

The first designed, well defined molecular water oxidation catalyst was the Ru "blue dimer" reported by Meyer and coworkers, $[(bpy)_2(OH_2)Ru^{III}ORu^{III}(OH_2)(bpy)_2]^{4+}$ where bpy is 2,2′-bipyridine, ($[(OH_2)\mathbf{Ru^{III}ORu^{III}}(OH_2)]^{4+}$).[1a,b] Unfortunately, it undergoes rapid deactivation due to electron-transfer-induced anation, mainly at the $[(OH_2)\mathbf{Ru^{III}ORu^{IV}}(OH_2)]^{5+}$ stage.[2] This process is the result of the enhanced anion affinity of electron-deficient Ru^{IV} and the ease of oxidation of $[(OH_2)\mathbf{Ru^{III}ORu^{IV}}(X)]^{4+}$ compared to $[(OH_2)\mathbf{Ru^{III}ORu^{IV}}(OH_2)]^{5+}$.

Detailed studies with the Ru "blue dimer"[2] created the basis for the discovery that one side is enough for water oxidation catalysis, and pathways involving single-site catalysts have emerged.[3a-e] Recently, catalysts of the type [Ru(bda)(L)$_2$] (bda is 2,2′-bipyridine-6,6′-dicarboxylic acid; L is 4-picoline, pic, or isoquinoline, isq) reported by Sun and coworkers have received particular attention, Chart 1.[4a,b] These robust catalysts can oxidize water with turnover frequencies reaching values close to those needed for practical applications. According to these reports, O–O bond formation takes place by bimolecular oxyl radical coupling of two $[Ru^{V}=O]^{+}$ species generated by PCET oxidation of $[Ru^{IV}–OH]^{+}$.[4a]

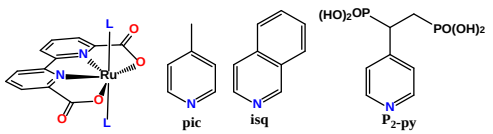

Chart 1. A. Structures of $[Ru^{II}(bda)(L)_2]$ (L = pic, isq, and P_2-py). See ESI for synthetic details.

We report here a combined solution-surface-DFT calculations study of the [Ru(bda)(L)$_2$] systems shown in Chart 1 that includes the X-ray structure of some of the intermediates in the catalytic cycle as well as pH-dependent electrochemistry in solution and with the catalyst anchored to metal oxide electrodes. These studies reveal that the bimolecular reaction takes place between two $[Ru^{IV}–OH]^{+}$ species rather than two $[Ru^{V}=O]^{+}$ molecules, generating a blue-dimer-like intermediate that has a high molar absorptivity and appears to be the active form of the catalyst.

Figure 1 shows cyclic voltammograms (CVs) for **[Ru(bda)(pic)$_2$]** in solution and for **[Ru(bda)(P$_2$-py)$_2$]** anchored on an FTO electrode in 0.1 M $HClO_4$. Two waves with equivalent peak currents are observed for **[Ru(bda)(pic)$_2$]** followed by a catalytic water oxidation wave. These were previously assigned as $[Ru^{III}–OH_2]^{+}/[Ru^{II}–OH_2]$, $[Ru^{IV}–OH]^{+}/[Ru^{III}–OH_2]^{+}$ and $[Ru^{V}=O]^{+}/[Ru^{IV}–OH]^{+}$ by Sun and coworkers.[4a] Note that $[Ru^{II}–OH_2]$ and $[Ru^{III}–OH_2]$ are 20 and 19-electron species, respectively, and violate the 18-electron rule. For **[Ru(bda)(P$_2$-py)$_2$]** the CV is strikingly different. The $Ru^{III/II}$ couple appears at lower potential due in part to the pH-dependence introduced on this couple by the phosphonic acid groups. The $Ru^{IV/III}$ couple is kinetically

inhibited and there is no catalytic water oxidation wave. Kinetic inhibition of $Ru^{IV/III}$ couples is common, and it is particularly noticeable with mono- or sub mono-layer coverage of complexes on planar electrodes.[3a,5] The lack of catalysis by **[Ru(bda)(P$_2$-py)$_2$]** in Figure 1 compared to **[Ru(bda)(pic)$_2$]** can be explained in terms of available mechanistic pathways for water oxidation catalysis for the two complexes. **[Ru(bda)(P$_2$-py)$_2$]** is site-isolated on the surface and most molecules only have access to single-site O–O bond formation for water oxidation, which is thermodynamically uphill for this catalyst. **[Ru(bda)(pic)$_2$]**, on the other hand, has access to bimolecular pathways between two catalyst molecules as proposed previously.[4a,b]

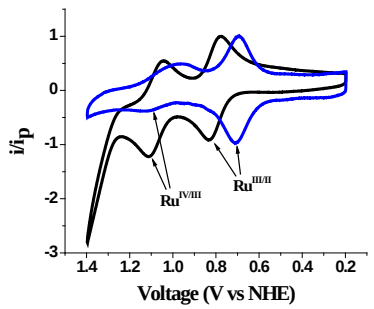

Figure 1. CVs for [Ru(bda)(pic)$_2$] (black trace) in solution with a glassy carbon electrode and [Ru(bda)(P$_2$-py)$_2$] (blue trace) on an FTO electrode in 0.1 M $HClO_4$. The currents have been normalized for $v^{1/2}$ and v, respectively, and then for the $Ru^{III/II}$ peak current.

The X-ray structure of **[Ru(bda)(pic)$_2$]** has been reported by Sun *et al.*[4b] There is a six coordinate, 18-electron environment around the Ru center. It could be argued that [Ru^{II}(κ^3-bda)(pic)$_2$(OH$_2$)] is in equilibrium with [Ru^{II}(κ^4-bda)(pic)$_2$], although the ^{1}H NMR for **[Ru(bda)(P$_2$-py)$_2$]** in D_2O (**[Ru(bda)(pic)$_2$]** is not soluble in pure D_2O) is symmetric, consistent with only [Ru^{II}(κ^4-bda)(pic)$_2$] in solution, see ESI. On the other hand, [Ru^{III}(κ^3-bda)(pic)$_2$(OH$_2$)]$^+$ is 1.2 kcal/mol lower in energy than [Ru^{III}(κ^4-bda)(pic)$_2$]$^+$ + H_2O based on DFT calculations for **[Ru(bda)(pic)$_2$]** (Figure S7, see ESI for details of DFT calculations). Bulk electrolysis in 0.1 M $HClO_4$ past the first oxidation wave for **[Ru(bda)(pic)$_2$]** in Figure 1 resulted in passage of ~ 1 eq of charge, consistent with a one-electron redox process. The resulting Ru^{III} intermediate was isolated as the perchlorate salt and characterized by single-crystal X-ray diffraction as [Ru^{III}(bda)(pic)$_2$](ClO_4), Figure S8. It is also a six coordinate structure, with no coordinated water molecule. Apparently, an equilibrium exists between [Ru^{III}(κ^3-bda)(pic)$_2$(OH$_2$)]$^+$ and [Ru^{III}(κ^4-bda)(pic)$_2$]$^+$ + H_2O in solution but less soluble [Ru^{III}(bda)(pic)$_2$](ClO_4) crystallizes preferentially. Table S1 shows a comparison of bond distances between [Ru^{II}(bda)(pic)$_2$] and [Ru^{III}(bda)(pic)$_2$]$^+$. The X-ray structure of [Ru^{III}(bda)(isq)$_2$](ClO_4), prepared by a similar procedure, is shown in Figure S9.

A CV of **[Ru(bda)(pic)$_2$]** in pH 8.0 phosphate buffer is shown in Figure S10. A single reversible wave is followed by a catalytic water oxidation wave. Note that the onset potential is significantly lower and the catalytic current is significantly larger compared to pH 1.0. The latter is indicative of base-assisted catalysis[6a-c] and arises because of the involvement of proton or proton-coupled electron transfer (PCET) in the rate determining step of the catalytic cycle. Figure S10 also shows a CV for **[Ru(bda)(P$_2$-py)$_2$]** on FTO under the same conditions, see figure caption for details. The inset shows an expansion of the $Ru^{V/IV}$ and $Ru^{IV/II}$ waves. In contrast to the homogeneous version, the "heterogeneous" anchored catalyst shows no catalysis. This result supports the involvement of a bimolecular step or steps in the catalytic cycle. On a planar surface, with site-isolated catalyst molecules, such pathways are inaccessible or significantly inhibited.

For **[Ru(bda)(pic)$_2$]** at low pH, the first redox process is a one-electron oxidation from six coordinate, 18-electron ^{1}[Ru^{II}] to six coordinate, 17-electron ^{2}[Ru^{III}(κ^4-bda)(pic)$_2$]$^+$, Figure S11. Based on DFT calculations, the latter is in equilibrium with ^{2}[Ru^{III}(κ^3-bda)(pic)$_2$(OH$_2$)]$^+$, which oxidizes at lower potential than ^{2}[Ru^{III}(κ^4-bda)(pic)$_2$]$^+$ and thus dominates the electrochemistry. This is followed by a PCET process from six-coordinate, 17-electron ^{2}[Ru^{III}(κ^3-bda)(pic)$_2$(OH$_2$)]$^+$ to seven coordinate, 18-electron ^{1}[Ru^{IV}–OH]$^+$, eq 1, up to ~ pH 5. Coordination expansion is enabled by a two-electron vacancy in d^4 [Ru^{IV}]$^{2+}$ compared to d^6 [Ru^{II}] and d^5 [Ru^{III}]$^+$ and by the wide N–Ru–N angle. The structure and ground state of ^{1}[Ru^{IV}–OH]$^+$ has been confirmed by Sun and coworkers by single-crystal X-ray diffraction and ^{1}H-NMR spectroscopy, respectively.[4b] The last redox process in Figure S11 has been previously assigned as the PCET oxidation of 18-electron ^{1}[Ru^{IV}–OH]$^+$ to 17-electron ^{2}[Ru^{V}=O]$^+$.[4a] A different assignment is presented here, see below. An interesting transition takes place in the Pourbaix diagram above pH 5 that also differs from a previously reported result.[4a] The dominant species becomes ^{3}[Ru^{IV}=O] (more stable than ^{1}[Ru^{IV}=O] by 23.9 kcal/mol based on DFT calculations) instead of ^{1}[Ru^{IV}–OH]$^+$ and the second redox process becomes a 1e$^-$/2H$^+$ process with a slope of ~ -118 mV/pH unit between pH 5 and 6. Around pH 6, another interesting transition takes place. The pH-dependent oxidation of ^{2}[Ru^{III}–OH$_2$]$^+$ to ^{3}[Ru^{IV}=O] crosses below pH-independent oxidation of ^{1}[Ru^{II}] to ^{2}[Ru^{III}]$^+$ and a single 2e-/2H$^+$ process takes ^{1}[Ru^{II}] to ^{3}[Ru^{IV}=O] with the slope again becoming –59 mV/pH unit. A significant implication of this transition is that ^{2}[Ru^{III}]$^+$ becomes unstable with respect to disproportionation to ^{1}[Ru^{II}] and ^{3}[Ru^{IV}=O]. Solutions of ^{2}[Ru^{III}]$^+$ in 0.1 M TFA (pH < 2) are stable for minutes to hours, but increasing the pH to 7.0 by mixing with 0.2 M, pH 7.0 phosphate buffer results in a very fast reaction (presumably disproportionation of ^{2}[Ru^{III}]$^+$) followed by slower competing reactions that lead to a mixture of products. Interestingly, the spectroscopic signature of the dominant product (λ_{max} = 688 nm with high absorptivity) closely resembles the absorption spectrum of the III-III form of the blue dimer, [(OH$_2$)**Ru^{III}ORu^{III}**(OH$_2$)]$^{4+}$, particularly that of the carboxylated analogue with 2,2′-bipyridine-4,4′-dicarboxylic acid reported by Grätzel and coworkers (λ_{max} = 678 nm).[7] The culprit in the generation of these species appears to be Ru^{IV}, either as ^{3}[Ru^{IV}–OH]$^+$ (< pH 5) or as ^{3}[Ru^{IV}=O] (> pH 5, see the spectroelectrochemistry section below).

The Pourbaix diagram for **[Ru(bda)(P$_2$-py)$_2$]** on FTO is shown in Figure S12. It is topologically similar to the one for **[Ru(bda)(pic)$_2$]** with some minor differences. The first difference is the slight pH-dependence in the $Ru^{III/II}$ couple. This behavior has been observed before for phosphonated [Ru(bpy)$_3$]$^{2+}$ complexes[8] and for chromophore-catalyst assemblies incorporating phosphonated [Ru(bpy)$_3$]$^{2+}$-like chromophores.[9a,b] Two pK_a values (1.0 and 4.0) are discernible for the phosphonate groups of the **P$_2$-py** ligand. The second difference is the absence of a change in slope for the highest potential wave.

Figure 2 shows CVs for **[Ru(bda)(P$_2$-py)$_2$]** on high surface area *nano*-ITO[10] and planar FTO in 0.1 M $HClO_4$. For the latter the current has been multiplied by a factor of 10 to account for differences in current due to surface coverage. For the first wave, the only noticeable difference between the two electrodes is the peak to peak separation between the anodic and cathodic waves. This is a reflection of the higher conductivity of the planar electrode. For the second and third waves, the differences between the two electrodes are remarkable, with significant current enhancements in the higher surface area electrode. Current enhancements for the $Ru^{IV/III}$ wave on *nano*-ITO *vs* planar electrodes have been reported previously.[11]

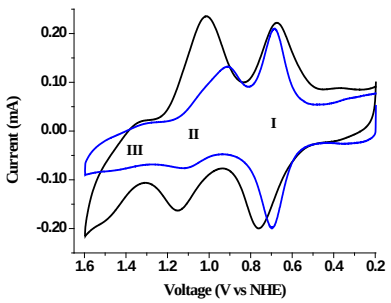

Figure 2. CVs for [Ru(bda)(P$_2$-py)$_2$] on *nano*-ITO (black trace) and on FTO electrodes (blue trace) in 0.1 M $HClO_4$. The current has been multiplied by a factor of 10 for the latter.

To obtain a better understanding at the mechanistic level of the electrochemical behavior of these systems, we turned to spectroelectrochemistry on *nano*-ITO.[10,11] Figure 3 shows spectroelectrochemical results for **[Ru(bda)(P$_2$-py)$_2$]** on *nano*-ITO in 0.1 M $HClO_4$. The potential was scanned in the anodic direction at 10 mV/s from 0 to 1.4 V and then cathodically back to 0 V with simultaneous absorption spectrum measurements every second. The pink trace shows the CV expressed as current *vs* time. Absorbance changes *vs* time at 3 selected wavelengths (382, 562 and 678 nm) are shown in black, red and blue, respectively. The absorbance at 382 and 562 nm decreases sharply as the Ru^{II} is oxidized to Ru^{III} (wave **I** in Figures 2 and 3, 20 to 75 s) consistent with the disappearance of MLCT absorptions associated with Ru^{II}. Simultaneously, the absorbance at 678 nm increases with an isosbestic point at 617 nm. This absorption band is not due to Ru^{III} but rather to a $\mathbf{Ru^{III}ORu^{III}}$ species. It is formed by disproportionation of Ru^{III} into Ru^{II} and Ru^{IV}–OH, followed by generation of $\mathbf{Ru^{IV}ORu^{IV}}$ from 2Ru^{IV}–OH and reduction to $\mathbf{Ru^{III}ORu^{III}}$ by Ru^{II}, see below. Spectral changes for this process are shown in Figure S13. Oxidation of Ru^{III} to "Ru^{IV}–OH" (wave **II** in Figures 2 and 3, 75 to 110 s) leads to unexpected spectral changes, Figure S14. A decrease in absorption at 678 nm is accompanied by an increase in absorption at 562 nm with the appearance of intense absorption bands at 440 and 562 nm and isosbestic points at 331, 387 and 640 nm. These spectral changes are not consistent with the formation of a Ru^{IV} monomeric species, see below and Figure S15, but with the formation of a Ru^{IV}–O–Ru^{IV} dinuclear species. TD-DFT calculations predict a band at 562 nm for the latter with similar molar absorptivity to the experimentally observed band (Figure S15). The last oxidation process (wave **III** in Figures 2 and 3, 110 to 140 s) results in a decrease in the absorbance at 562 nm and disappearance of the bands at 440 and 562 nm, Figure S16. It also marks the onset potential for O_2 generation, as determined by rotating ring-disc experiments, Figure S21.[12] These bands are recovered in the first reduction of the reverse scan from 141 to 170 s (return wave **III**) as shown by the growth of the absorbance at 562 nm in Figure 3. Their disappearance in the following reduction step from 172 to 216 s (return wave **II**) is accompanied by a steep increase in the absorbance at 678 nm and the growth of an intense band at 680 nm with an isosbestic point at 615 nm, Figure S17. This intense band at 680 nm is reminiscent of the absorption band observed for **[Ru(bda)(pic)$_2$]** in solution following disproportionation of the Ru^{III} species. It also resembles the spectrum of the III-III form of the blue dimer, $[(OH_2)\mathbf{Ru^{III}ORu^{III}}(OH_2)]^{4+}$ (λ_{max} = 678 nm).[7]

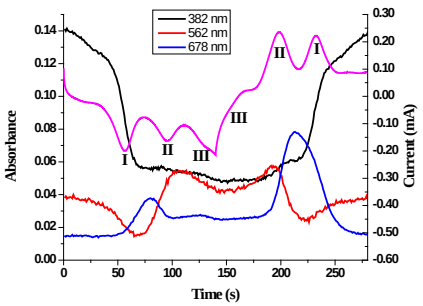

Figure 3. Spectroelectrochemical data for [Ru(bda)(P$_2$-py)$_2$] on *nano*-ITO in 0.1 M $HClO_4$. See text for explanation.

Finally, the last reduction step (217 to 280 s, return wave **I**) leads to a decrease of the absorbance at 678 nm and recovery of the absorbance at 382 nm and the MLCT bands of monomeric Ru^{II} with an isosbestic point at 588 nm. Spectral changes associated with this process are shown in Figure S18. Reduction of $[(OH_2)\mathbf{Ru^{III}ORu^{III}}(OH_2)]^{4+}$ in the blue dimer also leads to generation of two equivalents of monomeric Ru^{II}. Nevertheless, the behavior shown in Figure 3 for **[Ru(bda)(P$_2$-py)$_2$]** is completely reversible and the dinuclear species can be regenerated upon an anodic scan.

A very similar behavior is observed for **[Ru(bda)(pic)$_2$]** in solution. Controlled potential electrolysis at 1.2 V *vs* NHE (just past the $Ru^{IV/III}$ couple) in 0.15 M TFA results in the formation of a species **I** with relatively intense absorption bands in the visible with λ_{max} = 445 and 550 nm after passage of ~ 2 equivalents of charge, Figure S19. As for **[Ru(bda)(P$_2$-py)$_2$]** on *nano*-ITO, these absorption bands cannot be assigned to a monomeric Ru^{IV} species because the latter display very weak absorptions in the visible region. Instead, these features are consistent with the formation of a dinuclear species structurally similar to the Ru^{IV}–O–Ru^{IV} form of the blue dimer. DFT calculations show that these dinuclear species are accessible without significant steric encumbrance, Figure S15. To corroborate the formation of a dinuclear Ru^{IV}–O–Ru^{IV} species, controlled potential electrolysis was carried out at +0.97 V, a potential more negative than the $Ru^{IV/III}$ couple but more positive than the $Ru^{III/II}$ couple. Passage of ~1 equivalent of charge resulted in a color change from purple to blue-green with growth of an intense band at 672 nm. This is consistent with reduction of the Ru^{IV}–O–Ru^{IV} form of the dinuclear species to the corresponding Ru^{III}–O–Ru^{III} form, Figure S20.

The combined solution and surface studies presented here provide new and unexpected insight into the mechanism of water oxidation by [Ru(bda)(L)$_2$] and point to a very different mechanism from that previously proposed.[4a] These results are consistent with one-electron oxidation of six-coordinate [Ru^{II}(κ^4-bda)(L)$_2$] to six-coordinate [Ru^{III}(κ^4-bda)(L)$_2$]$^+$. The latter is in equilibrium with six-coordinate [Ru^{III}(κ^3-bda)(L)$_2$(OH$_2$)]$^+$ which oxidizes preferentially to seven coordinate [Ru^{IV}(κ^4-bda)(L)$_2$(OH)]$^+$. Generation of [Ru^{IV}–OH]$^+$ leads to a bimolecular reaction (k_2 in Scheme 1) to give the Ru^{IV}–Ru^{IV} form of a blue-dimer-like species. The proposed structure is based on spectroelectrochemistry, pH-dependent electrochemistry and DFT calculations. The intense absorption band at 672 nm in solution and 680 nm on *nano*-ITO can only be explained by invoking a strongly-coupled **Ru^{III}ORu^{III}** core.[2] One-electron oxidation of this dinuclear species will result in a Ru^{IV}–Ru^{V} species in a PCET process. As in the case of the blue dimer, the Ru^{IV}–Ru^{V} intermediate can be further oxidized to generate the corresponding Ru^{V}–Ru^{V} species, presumably followed by fast O–O coupling with oxygen release. The steps with rate constants k_2 and k_3 in Scheme 1 can be accelerated by bases owing to their PCET nature and this explains the base-assisted catalysis experimentally observed.

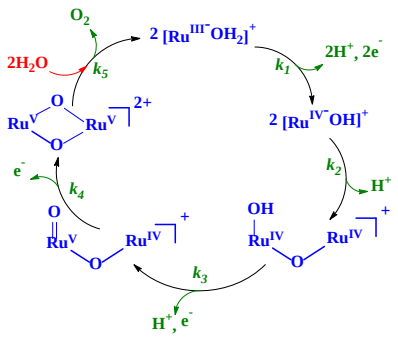

Scheme 1. Proposed water oxidation mechanism for [Ru(bda)(L$_2$)].

The two catalysts considered in this study appear to be the precursors of blue-dimer-like intermediates that are very active towards water oxidation catalysis. The interconversion between mono and dinuclear species is fast and reversible with [Ru^{IV}–OH]$^+$ or [Ru^{IV}=O] being the species involved in the bimolecular step. The anation problems responsible for deactivation of the catalytic activity of the blue dimer are avoided by having carboxylate groups around the metal centers that screen the charges of the high oxidation states and donate electron density to electron deficient Ru^{III}, Ru^{IV} and Ru^{V}. These studies also highlight both the mechanistic insight that can be gained by comparing solution and surface studies and the importance of catalysis studies with anchored catalysts in a true device configuration. In addition, the results presented here provide important insight for new catalysts design and protocols for incorporation of existing catalysts into solar cell devices for optimal performance.

This work was carried out at Brookhaven National Laboratory and supported by the U.S. Department of Energy, Office of Science, Division of Chemical Sciences, Geosciences, & Biosciences, Office of Basic Energy Sciences under contract DE-AC02-98CH10886.

Notes and references

[a] Department of Chemistry, Brookhaven National Laboratory. Email: jconcepc@bnl.gov

[b] Department of Natural Sciences, Baruch College, CUNY, New York, New York 10010.

[c] Present address: BASF, 500 White Plains Road, Tarrytown, NY 10591-9005 USA.

Electronic Supplementary Information (ESI) available: Experimental procedures, computational details and additional data. See DOI: 10.1039/c000000x/

1 (a) C. W. Chronister, R. A. Binstead, J. Ni and T. J. Meyer, *Inorg. Chem.*, 1997, **36**, 3814-3815. (b) S. W. Gersten, G. J. Samuels and T. J. Meyer, *J. Am. Chem. Soc.*, 1982, **104**, 4029-4030.

(2) F. Liu, J. J. Concepcion, J. W. Jurss, T. Cardolaccia, J. L. Templeton and T. J. Meyer, *Inorg. Chem.*, 2008, **47**, 1727-1752.

(3) (a) Z. Chen, J. J. Concepcion, J. W. Jurss and T. J. Meyer, *J. Am. Chem. Soc.*, 2009, **131**, 15580-15581. (b) J. J. Concepcion, J. W. Jurss, J. L. Templeton and T. J. Meyer, *J. Am. Chem. Soc.*, 2008, **130**, 16462-16463. (c) J. J. Concepcion, M.-K. Tsai, J. T. Muckerman and T. J. Meyer, *J. Am. Chem. Soc.*, 2010, **132**, 1545-1557. (d) J. F. Hull, D. Balcells, J. D. Blakemore, C. D. Incarvito, O. Eisenstein, G. W. Brudvig and R. H. Crabtree, *J. Am. Chem. Soc.*, 2009, **131**, 8730-8731. (e) H.-W. Tseng, R. Zong, J. T. Muckerman and R. Thummel, *Inorg. Chem.*, 2008, **47**, 11763-11773.

(4) (a) L. Duan, F. Bozoglian, S. Mandal, B. Stewart, T. Privalov, A. Llobet and L. Sun, *Nat. Chem.*, 2012, **4**, 418-423. (b) L. Duan, A. Fischer, Y. Xu and L. Sun, *J. Am. Chem. Soc.*, 2009, **131**, 10397-10399.

(5) Z. Chen, A. K. Vannucci, J. J. Concepcion, J. W. Jurss and T. J. Meyer, *Proc. Natl. Acad. Sci. U. S. A.*, 2011, **108**, E1461-E1469.

(6) (a) Z. Chen, J. J. Concepcion, X. Hu, W. Yang, P. G. Hoertz and T. J. Meyer, *Proc. Natl. Acad. Sci. U. S. A.*, 2010, **107**, 7225-7229. (b) Y. M. Badiei, D. E. Polyansky, J. T. Muckerman, D. J. Szalda, R. Haberdar, R. Zong, R. P. Thummel and E. Fujita, *Inorg. Chem.*, 2013, **52**, 8845-8850. (c) D. E. Polyansky, J. T. Muckerman, J. Rochford, R. Zong, R. P. Thummel and E. Fujita, *J. Am. Chem. Soc.*, 2011, **133**, 14649-14665.

(7) P. Comte, M. K. Nazeeruddin, F. P. Rotzinger, A. J. Frank and M. Graetzel, *J. Mol. Catal.*, 1989, **52**, 63-84.

(8) M. R. Norris, J. J. Concepcion, C. R. K. Glasson, Z. Fang, A. M. Lapides, D. L. Ashford, J. L. Templeton and T. J. Meyer, *Inorg. Chem.*, 2013, **52**, 12492-12501.

(9) (a) D. L. Ashford, W. Song, J. J. Concepcion, C. R. K. Glasson, M. K. Brennaman, M. R. Norris, Z. Fang, J. L. Templeton and T. J. Meyer, *J. Am. Chem. Soc.*, 2012, **134**, 19189-19198. (b) J. J. Concepcion, J. W. Jurss, P. G. Hoertz and T. J. Meyer, *Angew. Chem., Int. Ed.*, 2009, **48**, 9473-9476. (c) M. R. Norris, J. J. Concepcion, Z. Fang, J. L. Templeton and T. J. Meyer, *Angew. Chem., Int. Ed.*, 2013, **52**, 13580-13583.

(10) P. G. Hoertz, Z. Chen, C. A. Kent and T. J. Meyer, *Inorg. Chem.*, 2010, **49**, 8179-8181.

(11) Z. Chen, J. J. Concepcion, J. F. Hull, P. G. Hoertz and T. J. Meyer, *Dalton Trans*, 2010, **39**, 6950-6952.

(12) J. J. Concepcion; R. A. Binstead; L. Alibabaei; T. J. Meyer, *Inorg. Chem.* **2013**, *52*, 10744.